Small Reflectors for Ground Motion Monitoring With InSAR

Prabu Dheenathayalan, *Member, IEEE*, Miguel Caro Cuenca, Peter Hoogeboom, and Ramon F. Hanssen, *Senior Member, IEEE*

***Abstract*— In recent years, synthetic aperture radar interferometry has become a recognized geodetic tool for observing ground motion. For monitoring areas with low density of coherent targets, artificial corner reflectors (CRs) are usually introduced. The required size of a reflector depends on radar wavelength and resolution and on the required deformation accuracy. CRs have been traditionally used to provide a high signal-to-clutter ratio (SCR). However, large dimensions can make the reflector bulky, difficult to install and maintain. Furthermore, if a large number of reflectors are needed for long infrastructure, such as vegetation-covered dikes, the total price of the reflectors can become unaffordable. On the other hand, small reflectors have the advantage of easy installation and low cost. In this paper, we design and study the use of small reflectors with low SCR for ground motion monitoring. In addition, we propose a new closed-form expression to estimate the interferometric phase precision of resolution cells containing a (strong or weak) point target and a clutter. Through experiments, we demonstrate that the small reflectors can also deliver displacement estimates with an accuracy of a few millimeters. To achieve this, we apply a filtering method for reducing clutter noise.**

***Index Terms*— Artificial corner reflectors (CRs), deformation monitoring, infrastructure monitoring, interferometric phase precision, radar interferometry, remote monitoring, small reflectors, synthetic aperture radar (SAR).**

I. Introduction

THE limitation of synthetic aperture radar interferometry (InSAR) to monitor ground displacement in nonurban areas is usually solved by introducing coherent targets. Although originally designed for calibration purposes, artificial corner reflectors (CRs) are traditionally used as coherent targets in InSAR applications due to their large radar cross section (RCS) and wide RCS pattern [1]–[4]. With CRs, measurements with accuracy in the order of 1 mm have been demonstrated [5]. Traditionally, CRs have been designed to provide a very strong, dominant reflection compared with the background signal, which assures a high signal-to-clutter ratio (SCR) signal [6]. Small reflectors do not provide such high SCR values, but they are appealing for other reasons. First, their costs are lower. In the cases where a large number of reflectors are neededfor monitoring long infrastructures, such as oil pipe lines or grass-covered dikes, very low-cost reflectors are preferable. Second, their small dimensions make installation easier, particularly for infrastructure with reduced space. Third, small reflectors have a low visual impact on the landscape. In this paper, we study small reflectors and derive an expression for phase precision covering high and low SCR targets. Furthermore, we provide a design of a small bidirectional reflector tile (RT) and show how reduced size reflectors can deliver accurate observations when correctly filtered. Preliminary results of this paper have been presented in [7]. This paper is arranged as follows. In Section II, we briefly discuss and derive a new theoretical expression for phase variance as a function of its SCR, and we present a formula to calculate the RCS of RTs used in this paper. In Section III, we provide a design of small bidirectional reflectors that can be used for both ascending and descending passes. We also show a filtering approach that can deliver an increase in the signal-to-noise ratio (SNR) directly proportional to the square root of the number of CRs used in the filter. In Section IV, we describe the result of testing these small, bidirectional reflectors in a real situation. The formation scheme for measuring deformation is shown, and measurement results are demonstrated using TerraSAR-X data acquired over a test site in the Netherlands.

Manuscript received March 7, 2017; revised June 16, 2017; accepted July 14, 2017. Date of publication September 4, 2017; date of current version November 22, 2017. This work was supported in part by Liander through the TU Delft project Monitoring Surface Movement in Urban Areas Using Satellite Remote Sensing and in part by TNO through the Space Dikes Program. *(Corresponding author: Prabu Dheenathayalan.)*

P. Dheenathayalan, P. Hoogeboom, and R. F. Hanssen are with the Department of Geoscience and Remote Sensing, Delft University of Technology, 2628 CN Delft, The Netherlands (e-mail: p.dheenathayalan@tudelft.nl).

M. Caro Cuenca is with the Department of Radar Technology, Netherlands Organization for Applied Scientific Research, TNO, 2597 AK The Hague, The Netherlands.

Color versions of one or more of the figures in this paper are available online at http://ieeexplore.ieee.org.

Digital Object Identifier 10.1109/TGRS.2017.2731424

II. Signal-to-Clutter Ratio and the Phase Statistics

A. Phase Precision of Radar Targets

An SCR is a common metric for describing the quality of a radar observation [8, pp. 403–423]. When using the SCR for quality description, it is generally assumed that a target inside a resolution cell is the only object providing coherent information, whereas all other reflecting objects—the clutter—change randomly, which causes speckle [9]. In this paper, the term clutter noise is used to refer to the magnitude of the speckle (in power units). An SCR is defined as

$$\mathrm{SCR} = \frac{P_P}{P_C} \tag{1}$$

where P_P is the power reflected by the reflector (point target) and P_C is the power reflected by the clutter. The phase value of

0196-2892 © 2017 IEEE. Translations and content mining are permitted for academic research only. Personal use is also permitted, but republication/redistribution requires IEEE permission. See http://www.ieee.org/publications_standards/publications/rights/index.html for more information.

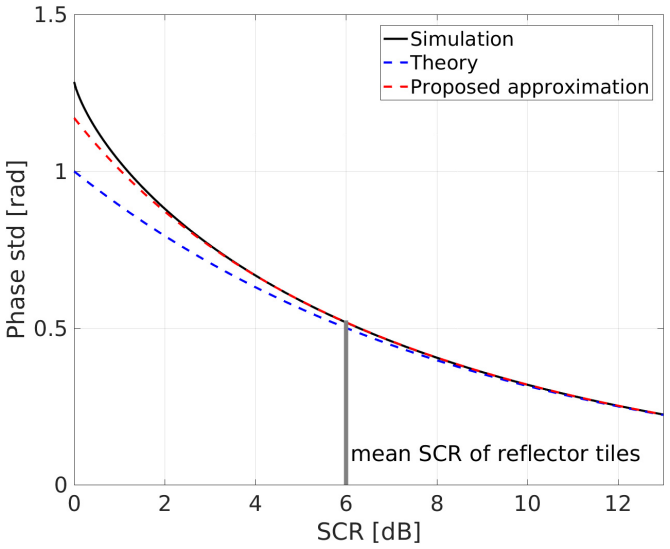

Fig. 1. Standard deviation of interferometric phases (single differences) determined using (2) (blue dashed line), our approximation (9) (red dashed line) and simulations (black solid line). The approximation given by (9) provides a good match with the simulations for SCR > 1 dB. The SCR of the RTs used in this paper is also indicated. We simulated an SCR for values down to 0 dB. Smaller values are possible, but considered of no interest, because the clutter power will dominate the cell.

the reflector, which is required in interferometric applications, is disturbed by the clutter to an extent depending on the magnitude of SCR. For high SCR objects, the influence of clutter variations is small, because P_P dominates over P_C. For traditional radar applications, such as target detection, a threshold of 13-dB SCR is commonly used [8]. For InSAR applications, such as subsidence monitoring, an SCR has been used as an indicator for the standard deviation of the interferometric phase, which is directly linked to the accuracy of the measurement, e.g., ground displacements [10]. For high SCR values, the interferometric phase standard deviation is given by [11], [12]

$$\sigma_\phi \approx \frac{1}{\sqrt{\text{SCR}}}. \tag{2}$$

σ_ϕ can be converted to the standard deviation of deformation σ_d by

$$\sigma_d = \sigma_\phi \cdot \frac{\lambda}{4\pi} \tag{3}$$

where λ is the radar wavelength. In this paper, we are mostly interested in reflectors that have low SCR values, but greater than 1. To test the validity of (2) for low SCR reflectors, we simulated a target plus random clutter as a coherent summation of point scatterers and compared the result with (2). Fig. 1 shows the result of this simulation. We find that (2) represents very well the standard deviation of the interferometric phase for the values of SCR above 10 dB. Below this value, (2) underestimates the experimentally derived standard deviation. Larger differences between (2) and simulations are found as the SCR decreases with a maximum of about 0.28 rd at an SCR of 0 dB. For this purpose, a new closed-form expression covering the phase precision of low and high SCR

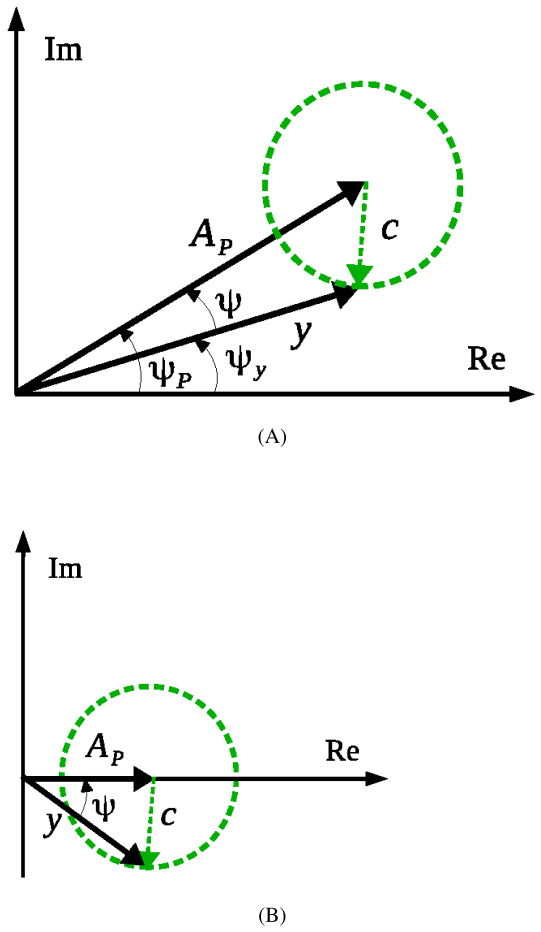

Fig. 2. Impact of clutter c (dotted curve) in a resolution cell with a dominant point scatterer (with amplitude A_P and phase Ψ_P) drawn in real (Re) and imaginary (Im) planes. (A) High SCR case, the stronger the point target A_P, the weaker the impact of clutter c on the phase $\Psi_y = \Psi - \Psi_P$. (B) Impact of the clutter in a resolution for a lower SCR case. The choice of point target phase is arbitrary and here, kept at $\Psi_P = 0$ for convenience.

targets is derived in this paper. Although, in radar applications, an SCR threshold of 13 dB is usually applied for the target detection [8], we find from simulations that interferometric phases for resolution cells with an SCR below this threshold are not strongly disturbed by clutter, and information contained in their reflections can still be extracted, despite the fact that such targets are hardly visible in a radar image. However, we have to consider that (2) represents only clutter noise. Thermal receiver noise and other noise types, e.g., atmospheric, system, and processing noise, are not considered. The actual interferometric phase standard deviation in a real measurement will therefore be higher than the value shown in Fig. 1.

For a single-look complex (SLC) SAR image, the complex return y (with amplitude $|y|$ and phase Ψ_y) from a resolution cell containing a dominant scatterer and a fully developed clutter can be written by

$$y = A_P \cdot e^{j\Psi_P} + c \tag{4}$$

where c is a complex number (with amplitude $|c|$ and a uniform distributed phase) representing a fully developed clutter (noise), and $|.|$ is the magnitude operator. For homogeneous

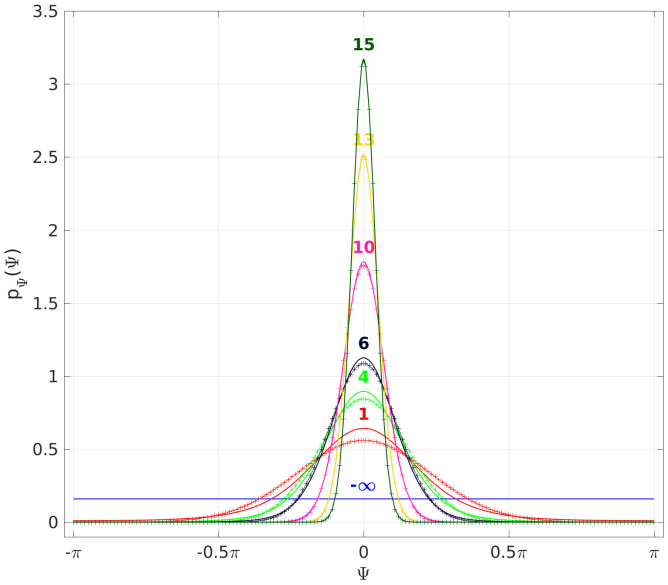

Fig. 3. PDF $p_\Psi(\Psi)$ of the SLC phase Ψ (in radians). The color lines represent the pdf (6) for different SCR values (in dB), and the crosses are their respective approximations given by (7). When SCR $=$ 0, i.e., $-\infty$ dB (resolution cell with only clutter), the pdf becomes an uniform distribution (blue line). The phase pdf given by (7) provides a reasonable approximation for a range of SCR $>$ 1 dB.

areas, i.e., the case of a fully developed speckle, the clutter exhibits a circular Gaussian distribution [13]–[18]. A_P and Ψ_P are the amplitude and phase of a point scatterer, respectively. The impact of one realization of clutter is shown in Fig. 2. Fig. 2(A) shows the impact for a high SCR case, and the phase of the resolution cell is less dependent on the clutter for high SCR values. For a low SCR resolution cell, the impact of clutter on phase is inevitable as shown in Fig. 2(B). From Fig. 2, the phase contribution of (a realization of) clutter in a resolution cell can be written geometrically as

$$\Psi = \arccos\left(\frac{A_P^2 + |y|^2 - |c|^2}{2A_P|y|}\right). \tag{5}$$

In general, the clutter contribution c is treated as a stochastic process. Therefore, the probability density function (pdf) of the SLC phase of a resolution cell in Fig. 2 can be written as [19, pp. 396–437]

$$p_\Psi(\Psi) = \frac{e^{-\mathrm{SCR}}}{2\pi}(1 + \beta\sqrt{\pi}\cdot e^{\beta^2}\cdot(1+\mathrm{erf}(\beta))) \quad \text{with}$$
$$\beta = \sqrt{SCR}\cdot\cos(\Psi - \Psi_P), \quad \forall\ -\pi \le \Psi - \Psi_P \le \pi \tag{6}$$

where erf(.) is the Gauss error function defined by $\mathrm{erf}(\alpha) = (2/\sqrt{\pi})\int_0^\alpha e^{-x^2}dx$. Here, the choice of dominant scatterer phase Ψ_P is arbitrary and hence set to zero as shown in Fig. 2(B). Therefore, substitute $\beta = \sqrt{\mathrm{SCR}}\cdot\cos(\Psi)$ in (6). The pdf of single-look phase for several values of SCR is plotted as colored lines in Fig. 3, and the colored crosses represent their Gaussian equivalents. It can be noted that the mean of the pdf is centered at $\Psi_P = 0$. When the signal contribution from the dominant scatterer vanishes (SCR $= -\infty$ dB), the resolution cell has only the clutter part, and the phase pdf approaches a uniform distribution (see blue line in Fig. 3). The pdf in (6) can be numerically approximated by

$$p_\Psi(\Psi) \approx \frac{1}{\sqrt{4\pi\,\mathrm{SCR} - \sqrt{3}}}\cdot e^{\frac{-\pi\ \Psi^2}{4\pi\,\mathrm{SCR}-2\sqrt{3}}}$$
$$\forall\ -\pi \le \Psi \le \pi, \text{ and } \mathrm{SCR} > \frac{\sqrt{3}}{2\pi}. \tag{7}$$

Equation (7) is a zero mean ($\Psi_P = 0$) Gaussian phase pdf with variance given by

$$\sigma_\Psi^2 = \frac{\pi}{2\pi\,\mathrm{SCR} - \sqrt{3}}. \tag{8}$$

The approximated pdf of (7) is plotted against the full pdf (6) in Fig. 3. From Fig. 3, we see that pdf approximation given by (7) (colored crosses) matches very well with the true pdf of (6) for the values of SCR $>$ 1 dB. But, for the case of SCR $\le$ 1 dB, the pdf approximation cannot fully describe the pdf (6). However, the proposed approximation is more than sufficient for the small RTs proposed in this paper, as their SCR is in the order of 5–6 dB. Now, for the reflectors with SCR $>$ 1 dB, the standard deviation of the interferometric phase ϕ of a resolution cell for the single-look case can be written from (8)

$$\sigma_\phi = \sqrt{2}\sigma_\Psi = \sqrt{\frac{2}{2\mathrm{SCR} - \sqrt{3}/\pi}} \approx \sqrt{\frac{2}{2\mathrm{SCR} - 0.55}}. \tag{9}$$

The proposed expression for σ_ϕ is plotted in red dashed line in Fig. 1. Comparing the red line [proposed expression, (9)] and blue line [theory, (2)] with the black line (simulated) in Fig. 1, one realizes that (9) provides an improved estimation of the interferometric phase precision for both low and high SCR targets when compared with the high-SCR approximation given by (2). In this paper, we used (9) to obtain the phase precision of the low-SCR targets, such as RT.

The estimation of a reflector SCR prior to its installation is a basic requirement in order to optimize design and resources. We estimate an SCR of a (point target) RT, $S_{\text{reflector}}$, from the ratio of RCS of the reflector to the expected RCS of the background clutter at the RCS location

$$\langle \mathrm{SCR}_{\text{reflector}} \rangle = \frac{\mathrm{RCS}_{\text{reflector}}}{\langle \mathrm{RCS}_{\text{clutter}} \rangle} \tag{10}$$

where $\langle\ \rangle$ is used to indicate the estimator operator, and $\mathrm{RCS}_{\text{reflector}}$ is deterministic.

In Sections II-B and II-C, we describe how to determine RCS for both the RTs and the clutter.

B. Radar Cross Section of Reflector Tiles

For simple objects, the RCS can be calculated from their geometry. In this paper, we use a triangular trihedral reflector, whose aperture forms an isosceles triangle, as shown in Fig. 4. Note that the sides b and a are different being $b > a$. This is a design choice we made to optimize the angular reflection pattern (the maximum reflection is required in the direction of the satellite) and the available space while maximizing the RCS (see Section III-A).

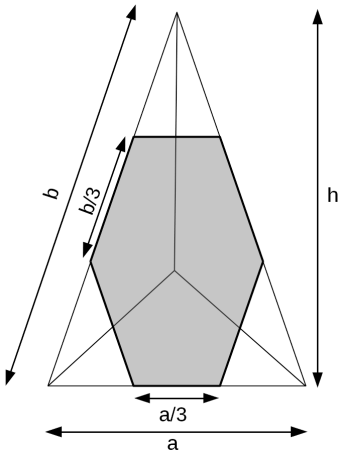

Fig. 4. Triangular trihedral reflector used in this paper with $b > a$. The effective aperture, A_{effec}, is shown as a gray irregular hexagon.

The effective aperture of a triangular trihedral reflector, A_{effec}, is determined from the portions of the surface that participate in the triple bounce mechanisms [20]. A_{effec} is shown in Fig. 4 as a gray irregular hexagon. The relationship between RCS and A_{effec} is given by

$$\text{RCS}_{\text{reflector}} = \frac{4\pi \cdot A_{\text{effec}}^2}{\lambda^2}. \tag{11}$$

The effective aperture can be calculated as follows:

$$A_{\text{effec}} = \frac{a \cdot h}{2} - \frac{a \cdot h}{6} = \frac{a \cdot h}{3} \tag{12}$$

where a and h are as indicated in Fig. 4. Note that h and b are related through Pythagoras's theorem, but we use h for convenience. The reflector RCS now becomes

$$\text{RCS}_{\text{reflector}} = \frac{4\pi \cdot a^2 \cdot h^2}{9\lambda^2}. \tag{13}$$

It is worth noting that in the case where the sides are equal $h = a\sqrt{3}/2$, and the RCS is given by

$$\text{RCS}_{\text{reflector}} = \frac{\pi \cdot a^4}{3\lambda^2} \tag{14}$$

which is the well-known RCS of a triangular trihedral reflector [20].

C. Radar Cross Section of the Background

The clutter RCS depends on the resolution of the radar and on the radar backscatter coefficient of the area

$$\text{RCS}_{\text{clutter}} = \sigma_0 \cdot A \tag{15}$$

where A is the ground area equal to the resolution cell, and σ_0 is the radar backscatter coefficient.

Models of σ_0 for different terrain types are reported in [21], which includes rocky terrain and short vegetation, among others. We have also access to the Dutch ROVE data set [22], which comprises many measurements of agricultural crops, grasses, and bare soils at the X-band and the Ka-band. We estimate the clutter RCS using the scattering model that was proposed in [21] for the case of terrain with short vegetation. The modeled σ_0 is given in dBm^2 per m^2 for different incidence angles, which can be easily adapted to the resolution and incidence angle provided by TerraSAR-X.

III. Small Reflectors for Ground Motion Monitoring

In this section, we provide the design of a small reflector that is optimized for ground motion monitoring. In Section III-A, the small bidirectional reflector is described. The expected SCR for these reflectors is analyzed in Section III-B.

Next, we investigate the challenges that are posed by the use of small reflectors due to their low SCR. In particular, we face two challenges for the case applying InSAR to ground motion monitoring. First, a small reflector is difficult to detect from a single image, especially if its SCR is less than 13 dB [8]. Second, the system noise plus clutter noise may dominate the radar returns, and so the signal of interest, such as the ground motion, may not be observed. To overcome those two limitations, we provide a method that consists of a deployment strategy and a filter (see Sections III-C and III-D).

A. Bidirectional Reflector Tiles Design

The reflector that we have designed for infrastructure monitoring is a bidirectional RT, as shown in Fig. 5. The tile includes two small trihedral CRs. One reflector is oriented to the ascending pass direction, and the other to the descending. Since they are connected to a unique tile structure, the reflectors are subject to the same ground displacement signal. Therefore, the RT can be easily applied for the estimation of a 2-D vector displacement. Note also that the reflectors aperture has a horizontal orientation to ease installation. The reflectors orientation plays obviously a major role, since we want the maximum RCS direction to coincide with the incidence angle θ_i of the satellite radar. Fig. 6 shows a crosscut of the reflector, where the angles and dimensions are defined. Through the selection of the rib sizes c and d, we have some freedom in selecting the maximum RCS direction while maintaining the horizontal aperture orientation. The ratio d/c determines the depression angle δ of the long rib c. The maximum RCS direction of the reflector with respect to rib c is θ. For a symmetrical CR ($c = d$), $\theta = 54°$. The value of θ increases with the ratio d/c as shown in Fig. 7.

The depression angle δ also increases with d/c. We may write the following relation:

$$\theta_i = 90° - \delta - \theta. \tag{16}$$

Fig. 7 shows the variation of θ_i, the direction of maximum RCS of the reflector, on the d/c ratio. By tuning the d/c ratio and the depression angle, the incidence angle required for a given sensor can be achieved. It is worth noting that the majority of radars operate with incidence angles between 20° and 50°. We constrained further the design with the second requirement on the thickness. We kept the thickness of the reflector (measured from apex to aperture) limited to ∼10 cm, and so it would fit in a top layer of a road for instance, which is usually in the order of 10–20 cm.

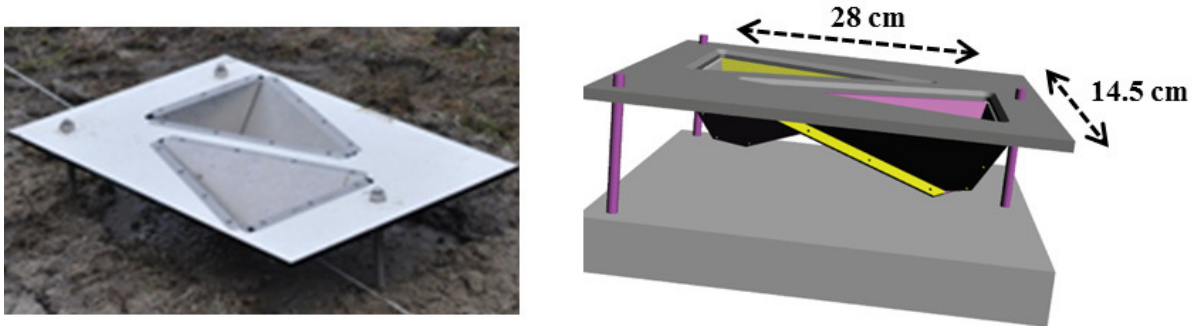

Fig. 5. Bidirectional RT, during (Left) installation and (Right) original design.

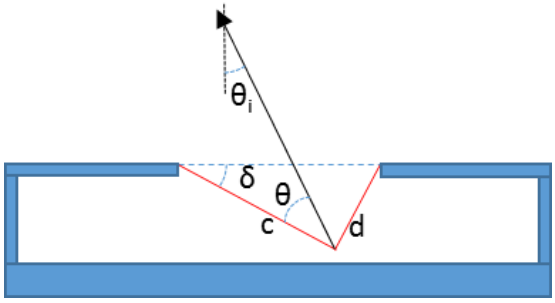

Fig. 6. Crosscut of the bidirectional RT, with one CR shown. The corner depression angle δ and the maximum RCS direction θ can both be influenced by the ratio of the corner ribs c and d.

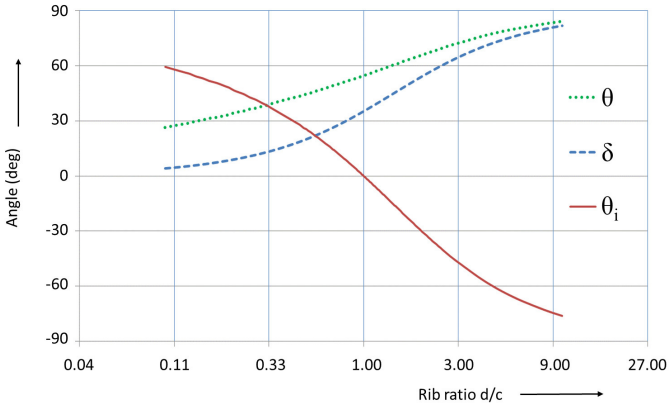

Fig. 7. Three parameters that depend on the corner rib ratio d/c are plotted. The corner depression angle δ and the angle of maximum RCS both increase with d/c. The resulting maximum RCS direction of the bidirectional RT decreases with d/c, spanning an angular range of more than 120°.

The bidirectional CR tile used in our experiment has dimensions $c = 28.2$ cm and $d = 14.5$ cm, resulting in a ratio $d/c = 0.51$. Hence, $\theta_i = 25.3°$. The wide elevation beamwidth of the CR provides sufficient flexibility to cover practical satellite radar incidence angle ranges. Fig. 8 shows the actual elevation diagrams for the bidirectional reflector. The beamwidth for each section is 45°. Note that for satellite incidence angles over 20°, only one section will produce a reflection. This ensures a single reflection from the bidirectional tile, leading to a stable and well-defined phase center. For angles smaller than 20°, both reflectors would contribute, leading to erroneous phase signals. In the design process, the minimum angle can be chosen as required. We have chosen the same d/c ratio for the two corners in the

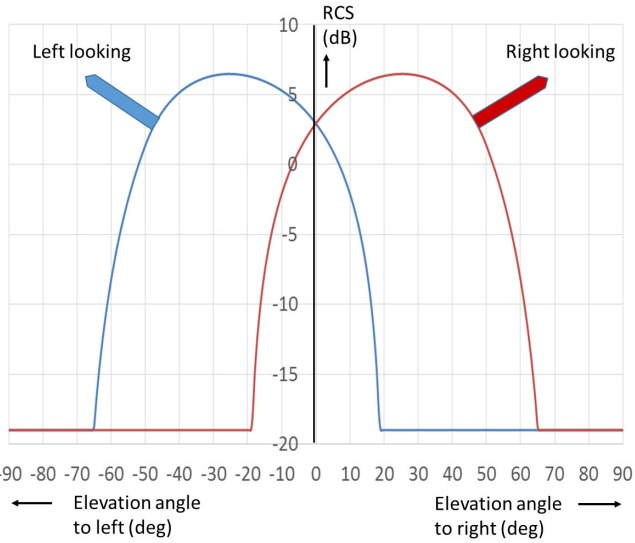

Fig. 8. Elevation diagram for the bidirectional reflector. Vertical look direction is 0_o. Left looking angles are negative, and right looking angles are positive. The responses of the two CRs are plotted separately. For incidence angles >20° (left and right looking), only one CR will respond to the radar, ensuring a well-defined phase center for the reflector.

bidirectional reflector, but it would be possible to use different ratios for both corners, in order to optimize the incidence angles for ascending and descending tracks of the satellite radar.

The maximum RCS of each reflector is 6.4 dBm^2, which is calculated using (13). The total dimensions of the tile are around 35 cm × 20 cm, with a height of 12 cm (excluding support base), similar to a pavement tile. The RT was designed to monitor grass-covered dikes, which are very common in the Netherlands and other low-land countries. A hole is drilled at the bottom of each reflector to drain rain water. Though we did not test this, installing a radome is possible, and it is expected to introduce a loss between 1 and 1.5 dB [8].

B. Expected SCR

As previously explained, we estimate the reflector SCR prior to its installation using a model of the backscattering coefficient σ_0 and of the background where the reflector will be placed. Our test will be executed with TerraSAR-X images, with resolution 3×3 m, and the incidence angle varies between 24° and 39°. The σ_0 of terrain with short grass observed

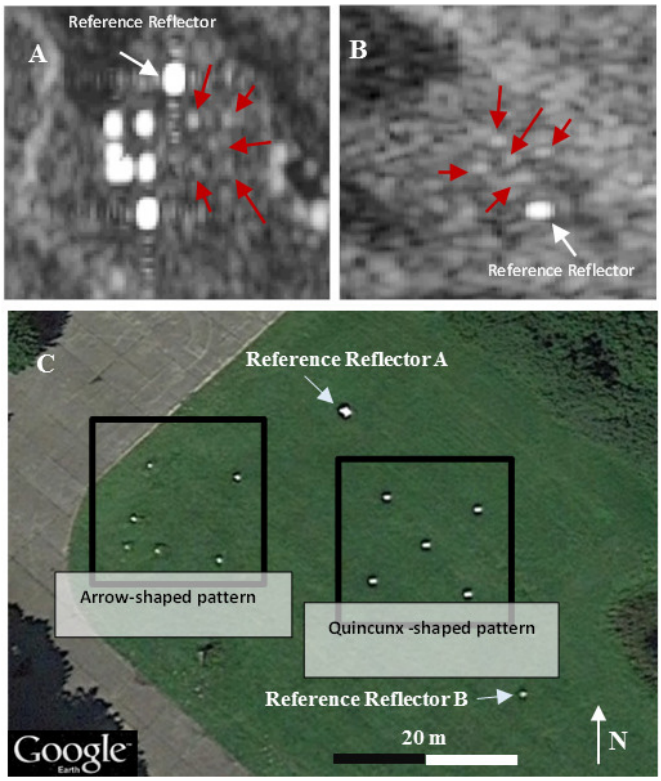

Fig. 9. Incoherent time-averaged SAR images for (A) descending and (B) ascending passes. RTs are indicated with red arrows. White arrows indicate reference reflectors, which are larger trihedral CRs. (C) Optical image (Google Earth [23]) of the area. RTs are deployed in a quincunx-shaped pattern. Other reflectors (trihedral ones) are deployed in an arrow-shaped pattern. These reflectors are not used in this paper and only visible in the descending pass [see (A)].

with an X-band radar at an incidence angle of 20°–40° is around -8 dBm^2/m^2 according to the Dutch ROVE data set [21], [22]. Now, the background RCS can be found from (15). The result is 1.5 dBm^2. Therefore, we expect a reflector SCR in the order of 4–5 dB. The value will not be the same for ascending and descending tracks, because the incidence angles are different and hence σ_0 will change slightly. Furthermore, the RCS of the CR at the satellite incidence angle of 39° is slightly reduced, as can be seen in Fig. 8.

Based on the estimated value of the SCR, we derive the first indication on the expected standard deviation using (9). An SCR of 5 dB is equivalent to a phase standard deviation of 0.6 rd, which provides about 1.5-mm line-of-sight (LOS) deformation precision (1σ confidence) for TerraSAR-X.

C. Reflector Tiles Deployment

We deploy the reflectors in a predefined and therefore recognizable pattern in order to precisely localize low SCR reflectors. The chosen pattern helps to both identify the reflectors within the SAR image and to yield an efficient method for spatial filtering. A matched filter can be used for fast and accurate localization of the reflectors within an SAR image. Fig. 9(C) shows deployment patterns that are used in the experiment.

Fig. 9(A) and (B) shows time-averaged amplitude images for (A) descending (30 images averaged) and (B) ascending passes (20 images averaged). Small reflectors forming a quincunx-shaped pattern are marked with red arrows. Because of their low SCR, the reflectors are almost undistinguishable from the clutter. The predefined deployment pattern therefore helps in their detection. Other reflectors of larger size are deployed in an arrow-shaped pattern. They appear as a very bright points in the descending pass [see Fig. 9(A)]. The reflectors forming an arrow-shaped pattern are not used in this paper.

D. Filtering

We filter the data by taking the coherent mean of the complex signal of the five selected pixels. This is similar to the coherent integration that is performed in classical radar technology [8] to improve the SNR. For truly coherent signals in the presence of random noise, the SCR improvement is equal to the number of coherently summed samples. In the InSAR case, the coherent filter improves the SCR when all reflectors are subject to the same deformation signal. Furthermore, since the distance between them is short, the atmospheric delay experienced by the radar returns is negligible between the reflectors. With the complex mean, the signal that is common to all reflectors (i.e., ground deformation) adds up. However, the clutter noise reduces due to its random nature. Therefore, the increase in the SCR is equal to the number of reflectors included in the filter, which is the same as the number of integrated radar returns. In Section IV, we prove experimentally that, despite the low power returned by individual reflectors, coherent averaging greatly reduces phase noise.

IV. Experimental Results

To test the bidirectional reflectors, we deployed them forming a quincunx pattern, as shown in Fig. 9. The test site was located in the Netherlands, a TNO premise near to Delft with visibility from both ascending (incidence angle ∼39°) and descending (incidence angle ∼24°) passes. The reflectors were installed in a geophysically stable area in a grass field, thus resembling the setup for our final goal, which was monitoring dikes which have similar vegetated surfaces.

A. Setup

In order to place many small CRs in a predefined formation, the spatial distances between reflectors have to be carefully chosen. Distances should not be too short to avoid interference between reflectors. We found that the distance between the reflectors should be at least two resolution cells to avoid mutual reflector interference. In addition to that, the maximum distance between the reflectors should be smaller than the decorrelation distance expected for both the deformation and the atmospheric signal, otherwise the spatial filter is not effective. Finally, the orientation of the pattern is chosen such that the interference due to sidelobes (from the CRs in the formation) is minimal.

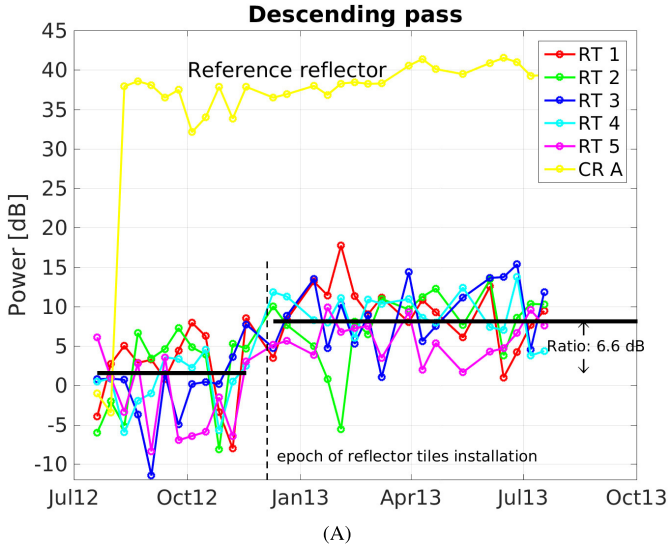

(A)

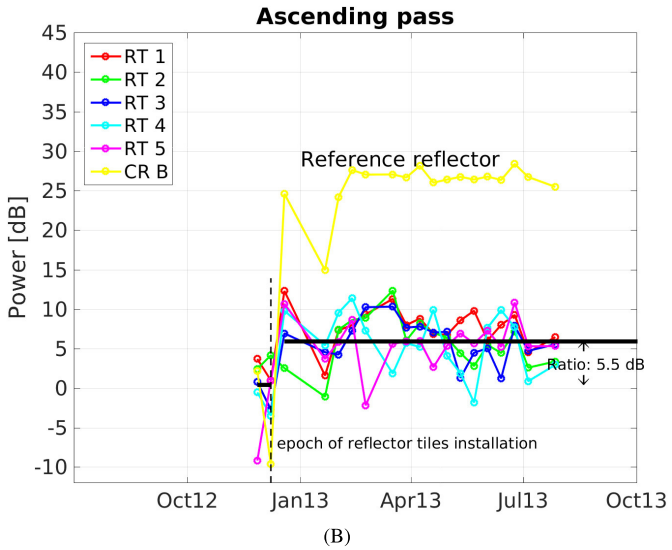

(B)

Fig. 10. Estimated SCR for tile reflectors (RT1–RT5) observed in the descending and ascending passes [red arrows in Fig. 9(A) and (B)]. The RTs were installed on December 5, 2012, indicated with a dashed line. The two horizontal black lines represent the average (linear, not dB averaged) power before and after installation of the RTs. The reference reflectors (of sides 1 m in descending and 45 cm in ascending) are traditional trihedral CRs (white arrows in Fig. 9). CR A and CR B were installed in August 2012 (for descending) and December 2012 (for ascending), respectively.

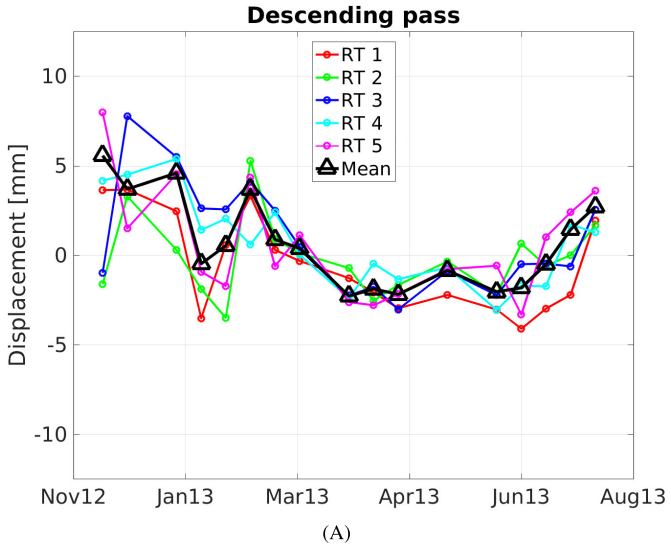

(A)

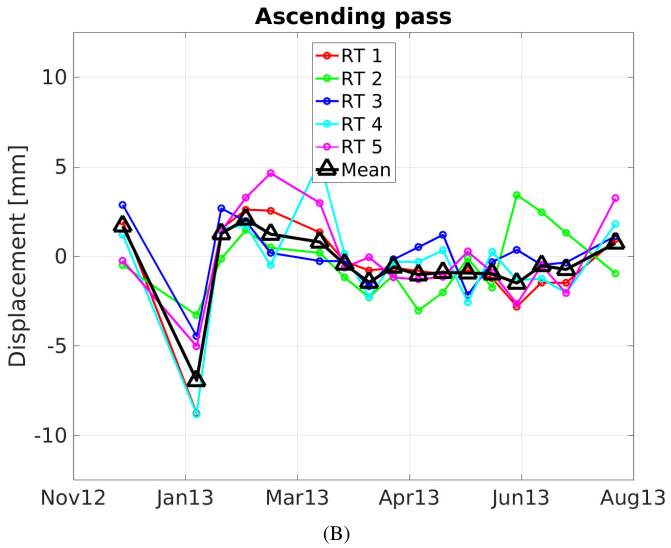

(B)

Fig. 11. Displacements estimated from interferometric phases for (A) descending and (B) ascending. Values represent motion with respect to the reference reflector. Mean value is shown with black triangles. Only observations after the installation of reflectors are included. The measured patterns in (A) and (B) differ due to their view angle and acquisition time differences. The ascending and descending passes were acquired with an incidence angle of ∼39° and ∼24°, respectively.

B. SCR Estimation

There exist different methods to estimate the SCR [22], and our approach is as follows. First, the clutter power is determined by taking the mean radar power of a small, and homogeneous area (with grass) before the reflector is installed. After the reflector is placed, we determine its response, which is the sum of the reflector and the clutter, and estimate the ratio of the two powers. Although clutter power will change over time, this method provides a reasonable approximation of the SCR, and the backscatter of the area is rather stable during wintertime when we performed this experiment. The power ratio determined by this way is

$$\frac{P_R + P_C}{P_C}. \tag{17}$$

The SCR was introduced in (1) as $S = P_R/P_C$, and can be easily calculated from the measured quantities. Clearly, the SCR will be smaller than the ratio in (17).

After the tiles were installed, the received power at the corresponding pixel positions increased ∼6 dB (see Fig. 10). As explained earlier, the SCR can now be estimated as 6 dB. This value is in agreement with the estimation in Section III-A.

From the radar detection theory, it is known that the reliable detection of a target requires an SCR of at least 13 dB [8]; hence, the tiles are ∼7 dB below detection threshold. In principle, this makes the RTs suitable for covert operations. To increase the RCS of the tiles to obtain an SCR of 13 dB, their size would have to be increased. Applying the same ratio, the sizes c and d in Fig. 6 would increase by a factor 1.6, from 14.5 cm ×28.2 cm to 23.2 cm ×45.1 cm, which is reasonably larger.

C. LOS Deformation Results

After the interferograms are formed with respect to a common master image and the contribution of the reference surface (the WGS84 ellipsoid) is removed [24], we calculate the interferometric phase differences of all RTs with respect to a reference reflector. A reference reflector with an SCR of around 37 dB (1-m sides) and 27 dB (45-cm sides) is used in descending and ascending, respectively, to avoid the addition of extra noise when taking double differences. The resulting phase differences are converted to radar LOS displacements. Fig. 11 shows the displacements for descending (A) and ascending (B) passes after the installation of the five RTs on the December 5, 2012. The phases of individual reflectors appear relatively stable, with the exception of the period around mid-January, when the reflectors were covered with snow. Note that despite the low SCR of individual reflectors (∼6 dB on average), the phase signal appears to be reasonably coherent. We reduce the phase noise by coherent averaging the five pixels in space as explained in Section III-D. The mean values of the interferometric phases of the reflectors are shown in Fig. 11 as black triangles for every measurement day. From Fig. 11, it is clearly visible that the variability of the signal of the mean is considerably less than those of individual reflectors.

Next, we estimate the improvement obtained from the filter. It is worth noting that the filter only works optimally if the phases are aligned in the sense that all reflectors included in the filter observed the same signal. In other words, the filter is optimal when the signal of interest (e.g., ground deformation) is spatially correlated and noise is not. For the noise variance estimation, we approximate the displacements with a linear plus seasonal model. After the removal of the estimated model, we determine a noise standard deviation of 3 mm for individual reflectors, the sensor wavelength being 31 mm. After the complex mean operation, we estimate a 1.5-mm standard deviation. The observations around the snow fall period (January 2013) are not used in the estimation of the standard deviation. The reduction in the standard deviation by a factor of 2 is in agreement with the expected theoretical improvement of $\sqrt{N}$, where N is the number of reflectors, equal to five in our case. We recall that the SCR improvement is a factor N, leading to a reduction in σ_ϕ of $\sqrt{N}$ [see (9)]. The estimated noise variances determined for this data set are probably overestimated, since they include unmodeled deformation, and other signals that are not true noise. In any case, this experimental setup measures the improvement obtained with the complex mean compared with their individual reflectors.

D. Decomposition of LOS Deformation

The bidirectional tiles enable the decomposition of the LOS deformation into horizontal and vertical displacement values. The TerraSAR-X observations were taken from two directions, ascending and descending passes at ∼39° and ∼24°, respectively. To find the vertical and horizontal displacements, we need to solve the following equations [24]:

$$\begin{bmatrix} d_{\text{desc}} \\ d_{\text{asc}} \end{bmatrix} = \begin{bmatrix} \cos(\theta_{\text{desc}}) & \sin(\theta_{\text{desc}}) \cdot \cos(\alpha_{\text{desc}}) \\ \cos(\theta_{\text{asc}}) & -\sin(\theta_{\text{asc}}) \cdot \cos(\alpha_{\text{asc}}) \end{bmatrix} \begin{bmatrix} V \\ H \end{bmatrix} \quad (18)$$

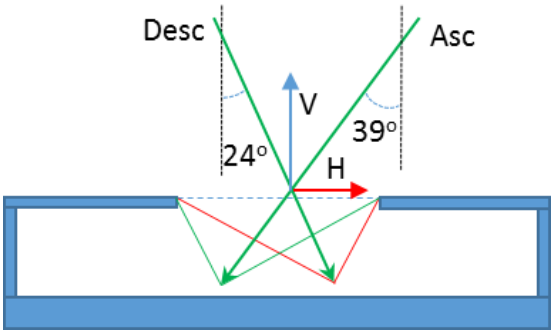

Fig. 12. Geometry of the observations in the plane through the two radar LOSs and their decomposition.

with d_{desc} and d_{asc} the displacement observed by the satellite in the descending mode and the ascending mode. θ_{desc} and α_{desc} are incidence and heading angles in the descending mode while θ_{asc} and α_{asc} are incidence and heading angles in the ascending mode. V and H are the vertical and horizontal (East) components, respectively. The heading angles of the satellite are 350° ($\alpha_{\text{asc}} = 10°$) for the ascending mode and 192° ($\alpha_{\text{desc}} = 12°$) for the descending mode. Since the radar looks perpendicular to the satellite track, the horizontal displacement in the east–west direction is the easiest to measure, whereas the one in the north–south direction may experience low accuracy. The vertical accuracy is dependent on the incidence angles. Fig. 12 shows the situation in a diagram.

In this case study, the observed displacements are expected to be mostly in the vertical direction. However, discrepancies between the signals observed at ascending and descending passes may occur due to a difference in the incidence angle between passes (∼39° and ∼24°, respectively) and different reference reflectors for ascending and descending passes. Different sampling times can also produce large variations between these two time series. For example, the snow fall in the beginning of January 2013 was closer in time to the ascending acquisition than to the descending one, as can be seen by comparing Fig. 11(A) and (B).

The estimated vertical and horizontal displacements are shown in Fig. 13. The plotted lines include both estimates, the ones obtained from individual reflectors (colored lines with circles) and also the estimate obtained after applying the complex mean filter (black line with triangles). The variances and covariance of vertical (V) and horizontal (H) components of the complex means are [from (18)] $\sigma_V^2 = 1.3^2$ mm^2, $\sigma_H^2 = 2.1^2$ mm^2, and $\sigma_{VH}^2 = 0.6^2$ mm^2, respectively. These values are smaller by a factor of N when compared with the individual tiles.

We observe a weak horizontal component. We attribute this to the noise floor, besides that we do not expect any motion of the RTs in the horizontal plane (based on the local conditions). In the vertical plane, we see a subsidence of the reflectors of several miilimeters in the first two months after installation. This could be a settling effect. The tiles were simply placed on a 10-cm layer of sand, which was compressed manually.

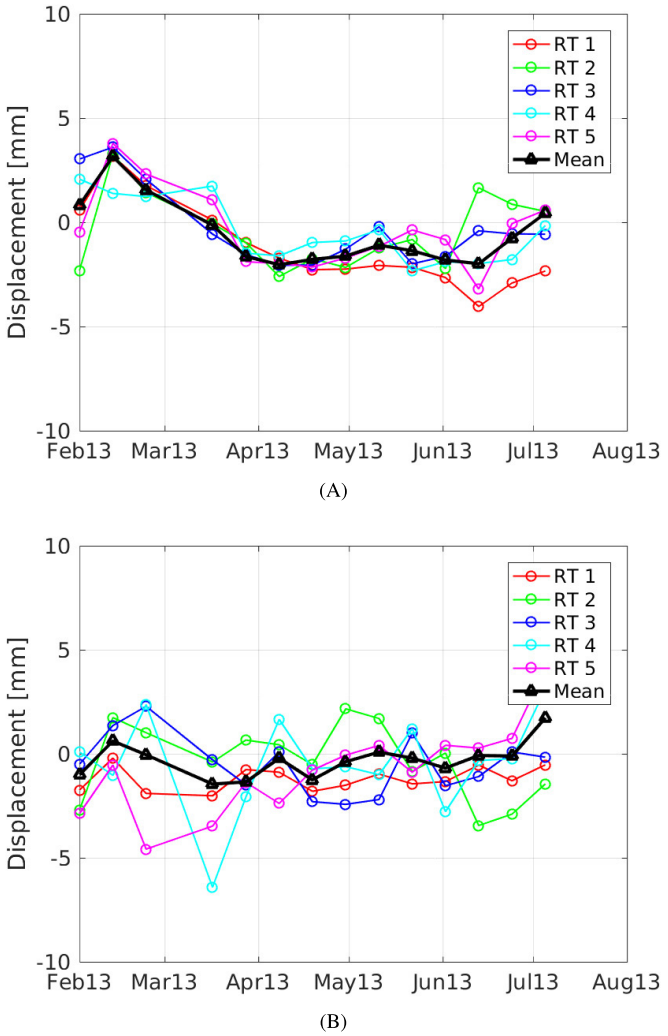

Fig. 13. (A) vertical and (B) horizontal displacement of the five RTs (RT1–RT5) as a function of time in the first half year of 2013. Black line with triangles represents the displacements after the signal is spatially filtered. Color lines with circles represent the estimations of vertical displacement and horizontal displacement for individual RTs RT1–RT5.

E. Discussion

The RTs that we propose in this paper were designed for monitoring grass-covered dikes and specifically developed for X-band satellites. We selected X-band satellites, because they provide high-resolution data and have small wavelengths enabling the use of small reflectors, which are cheap. Furthermore, there are a large number of X-band satellites, TerraSAR-X, CosmoSky-Med, and KOMPSAT5, that can help to reduce the observation time and improve the monitoring strategy. The deployment of reflectors should aim at optimizing the sampling of the ground deformation, but also taking into account that the distance between reflectors should be less than the decorrelation distance of atmospheric disturbances, i.e., around 800 m [25]. For reliable deformation interpretations, a good foundation for RT may be required. In those cases, care should be taken to avoid any settlement experienced due to the foundation. When monitoring infrastructures as natural dikes (e.g., peat dikes), we suggest positioning the reflectors near the dikes crown, since the upper part of the dike experiences the largest fluctuations. The final precision of the LOS estimation will depend on the number of reflectors included in the filter. For example, if the deformation signal does not change over an area where N reflectors are included in the spatial averaging filter, the expected precision is around $3/\sqrt{N}$ mm. Although developed for dike monitoring (e.g., grass- and vegetation-covered dikes), these bidirectional tiles are also well suited for other types of infrastructure, such as roads, large bridges, and dams, whose orientation is not optimal for the radar satellites.

V. Conclusion

We have shown that small CRs can be used for interferometric applications. However, due to their low SCR, they appear hidden in the clutter. By deploying the reflectors in predefined patterns, we were able to localize them in radar images, whereas the individual reflectors were invisible in a single image. They start to appear somewhat visible after applying a temporal filter on radar images power. Despite their low SCR, we have proved that small reflectors contain coherent information and that they are valuable for interferometric applications. A combination of small reflectors can be used to reduce SCR-induced errors in the interferometric phase or deformation signal. In addition, we have derived a new expression to estimate interferometric phase precision for resolution cells having a point target and clutter. From our experiments, we conclude that the complex mean of the interferometric signals improves the phase accuracy by a factor $\sqrt{N}$, being N the number of reflectors in the ensemble. We estimated for each RT $\sim$3 mm standard deviation of the interferometric phase noise, compared with $\sim$1.5 mm for the complex mean of five RTs. Noise includes all signals that are not included in the deformation model. We were able to decompose the LOS deformation signals of ascending and descending passes in horizontal and vertical displacements of the RTs with a standard deviation of about 2.1 and 1.3 mm, respectively. The structure of the RTs enabled this application in a favorable way.

Acknowledgment

The authors would like to thank the German Aerospace Center (DLR) for acquiring and providing TerraSAR-X time-series images over Delft. The authors would also like to thank the anonymous reviewers for their helpful comments.

References

[1] K. Sarabandi and T.-C. Chiu, "Optimum corner reflectors for calibration of imaging radars," *IEEE Trans. Antennas Propag.*, vol. 44, no. 10, pp. 1348–1361, Oct. 1996.

[2] D. Small, B. Rosich, E. Meier, and D. Nüesch, "Geometric calibration and validation of ASAR imagery," presented at the CEOS WGCV SAR Calibration Validation Workshop, Ulm Germany, May 2004.

[3] Y. Qin, D. Perissin, and L. Lei, "The design and experiments on corner reflectors for urban ground deformation monitoring in Hong Kong," *Int. J. Antennas Propag.*, vol. 2013, 2013, Art. no. 191685, doi: 10.1155/2013/191685.

[4] P. Dheenathayalan, D. Small, A. Schubert, and R. F. Hanssen, "High-precision positioning of radar scatterers," *J. Geodesy*, vol. 90, no. 5, pp. 403–422, May 2016. [Online]. Available: http://dx.doi.org/10.1007/s00190-015-0883-4

[5] A. Ferretti *et al.*, "Submillimeter accuracy of InSAR time series: Experimental validation," *IEEE Trans. Geosci. Remote Sens.*, vol. 45, no. 5, pp. 1142–1153, May 2007.
[6] A. Freeman, "Polarization effects and multipolarization SAR," in *Fundamental and Special Problems of Synthetic Aperture Radar (SAR)* (AGARDLS-182. NASA/JPL), Pasadena, CA, USA: Agard, Aug. 1992, pp. 5/1–5/13.
[7] M. C. Cuenca, P. Dheenathayalan, W. van Rossum, and P. Hoogeboom, "Deployment and design of bi-directional corner reflectors for optimal ground motion monitoring using InSAR," in *Proc. 10th Eur. Conf. Synth. Aperture Radar (EUSAR)*, Jun. 2014, pp. 1–4.
[8] M. I. Skolnik, *Introduction to Radar Systems*. Tokyo, Japan: McGraw-Hill, 1962.
[9] A. C. Frery, H.-J. Müller, C. C. F. Yanasse, and S. J. S. Sant'Anna, "A model for extremely heterogeneous clutter," *IEEE Trans. Geosci. Remote Sens.*, vol. 35, no. 3, pp. 648–659, May 1997.
[10] B. M. Kampes, *Radar Interferometry: Persistent Scatterer Technique*. Dordrecht, The Netherlands: Springer, 2006.
[11] J. W. Goodman, "Statistical properties of laser speckle patterns," in *Laser Speckle and Related Phenomena* (Topics in Applied Physics), vol. 9, J. Dainty, Ed. Heidelberg, Germany: Springer-Verlag, 1975, ch. 2, pp. 9–75.
[12] D. Just and R. Bamler, "Phase statistics of interferograms with applications to synthetic aperture radar," *Appl. Opt.*, vol. 33, no. 20, pp. 4361–4368, 1994.
[13] J. Dainty, Ed., *Laser Speckle and Related Phenomena* (Topics in Applied Physics), vol. 9. Heidelberg, Germany: Springer-Verlag, 1975.
[14] J. W. Goodman, "Some fundamental properties of speckle," *J. Opt. Soc. Amer.*, vol. 66, no. 11, pp. 1145–1150, Nov. 1976.
[15] S. Madsen, "Speckle theory: Modelling, analysis, and applications related to synthetic aperture radar data," Ph.D. dissertation, Electromagn. Inst., Tech. Univ. Denmark, Lyngby, Denmark, 1986.
[16] W. Davenport and W. Root, *An Introduction to the Theory of Random Signals and Noise*. New York, NY, USA: IEEE Press, 1987.
[17] G. Molesini, M. P. de Souza, F. Quercioli, and M. Trivi, "Experimental statistics of fully developed speckle fields by phase-shifting interferometry," *Opt. Commun.*, vol. 77, nos. 2–3, pp. 129–134, Jun. 1990.
[18] R. Bamler and P. Hartl, "Synthetic aperture radar interferometry," *Inverse Problems*, vol. 14, no. 4, pp. R1–R54, 1998. [Online]. Available: http://doris.tudelft.nl/Literature/bamler98.pdf
[19] D. Middleton, *An Introduction to Statistical Communication Theory* (International Series in Pure and Applied Physics), vol. 960. New York, NY, USA: McGraw-Hill, 1960,
[20] E. F. Knott, J. F. Shaeffer, and M. T. Tuley, *Radar Cross Section*. Norwood, MA, USA: Artech House, 1985.
[21] F. T. Ulaby and M. C. Dobson, *Handbook of Radar Scattering Statistics for Terrain*. Norwood, MA, USA: Artech House, 1989, p. 500.
[22] G. P. de Loor, P. Hoogeboom, and E. P. W. Attema, "The dutch ROVE program," *IEEE Trans. Geosci. Remote Sens.*, vol. GE-20, no. 1, pp. 3–11, Jan. 1982.
[23] GoogleInc. (2017). *Google Earth (Version 7.1.5.1557)*. [Online]. Available: http://www.earth.google.com
[24] R. F. Hanssen, *Radar Interferometry: Data Interpretation and Error Analysis*. Dordrecht, The Netherlands: Kluwer, 2001.
[25] F. Rocca, "Modeling interferogram stacks," *IEEE Trans. Geosci. Remote Sens.*, vol. 45, no. 10, pp. 3289–3299, Oct. 2007.

Prabu Dheenathayalan (M'08) received the B.E. (Sandwich) degree in electrical and electronics from the PSG College of Technology, Coimbatore, India, in 2005, and the M.Sc. degree in information and communication engineering from the Karlsruhe Institute of Technology, Karlsruhe, Germany, in 2009. He is currently pursuing the Ph.D. degree with the Department of Geoscience and Remote Sensing, Delft University of Technology, Delft, The Netherlands.

He was with Honeywell Technology Solutions from 2005 to 2007. During his master's degree, he was with Harman Becker Automotive Systems GmbH, Karlsruhe; and the German Aerospace Center (DLR), Weßling, Germany. He is also a Researcher with the Department of Geoscience and Remote Sensing, Delft University of Technology. He holds two granted patents. His research interests include remote sensing, SAR interferometry, and image/signal processing.

Miguel Caro Cuenca received the five-years bachelors degree in fundamental physics and applied physics from University of Granada, Granada, Spain, and Edinburgh Napier University, Edinburgh, U.K., respectively, in 2000, and the M.Sc. degree in microwave communication from the University of Portsmouth, Portsmouth, U.K., in 2001, and the Ph.D. degree in radar interferometry from the Delft University of Technology, Delft, The Netherlands, in 2012.

He was with Thales Nederland from 2004 to 2006, under the Marie Curie research. He joined the Delft University of Technology in 2006, initially as a Ph.D. Candidate and later as an Associate Researcher. Since 2012, he has been with Netherlands Organisation for Applied Scientific Research, TNO, The Hague, The Netherlands, as a Researcher, where he has been involved in the field of signal processing applied to radar.

Peter Hoogeboom received the M.S.E. degree in electrical engineering from the Delft University of Technology, Delft, The Netherlands, in 1975.

He was with the Netherlands Organisation for Applied Scientific Research, TNO, The Hague, The Netherlands, until 2014, where he was involved in microwave remote sensing and radar instruments, including SAR. He has been involved in the development of algorithms and applications for both civil and military needs. Since 1999, he has been a Professor in radar and Earth observation with the Delft University of Technology. Currently, he is with the Department of Geoscience and Remote Sensing, and he is involved in the studies among other atmospheric and earth applications, including interferometric SAR.

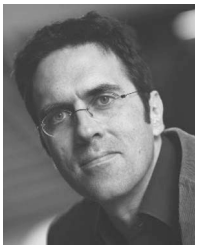

Ramon F. Hanssen (M'04–SM'15) received the M.Sc. degree in geodetic engineering and the Ph.D. *(cum laude)* degree from the Delft University of Technology, Delft, The Netherlands, in 1993 and 2001, respectively.

He was with the International Institute for Aerospace Survey and Earth Science, Stuttgart University, Stuttgart, Germany; the German Aerospace Center (DLR), Weßling, Germany; Stanford University, Stanford, CA, USA (Fulbright Fellow); and the Scripps Institution of Oceanography in microwave remote sensing, radar interferometry, signal processing, and geophysical application development. Since 2008, he has been an Antoni van Leeuwenhoek Professor in Earth observation with the Delft University of Technology, where he has been leading the Research Group on Mathematical Geodesy and Positioning since 2009. He has authored a textbook on radar interferometry.